Storm-time distortion of the inner magnetosphere: How severe can it get?

N. A. Tsyganenko

Universities Space Research Association and Laboratory for Extraterrestrial Physics, NASA Goddard Space Flight Center, Greenbelt, Maryland, USA

H. J. Singer

National Oceanic and Atmospheric Administration, Boulder, Colorado, USA

J. C. Kasper

Center for Space Research, Massachusetts Institute of Technology, Cambridge, Massachusetts, USA

[1]   First results are presented of an effort to model the storm-time distortion of the magnetic field in the inner magnetosphere using space magnetometer data. Strong geomagnetic storms are relatively rare events, represented by only a small fraction of the data used in the derivation of existing empirical geomagnetic field models. Hence using those models for the mapping of the storm-time magnetosphere is at most an extrapolation based on trends, obtained from quiet and moderately disturbed data. To overcome that limitation, a set of data was created, containing only clear-cut events with Dst $\leq$ −65 nT, with the goal to derive models of the inner and near geomagnetic field ($R < 15\ R_E$), representing strongly disturbed geomagnetic configurations and their evolution during the storm cycle. The final data set included about 143,000 records with 5-min average B-vectors, covering 37 major storms between 1996 and 2000. Most of the data came from GOES-8, -9, -10, Polar, and Geotail spacecraft, and two storms in February–March of 1998 were also partially covered by the data of Equator-S. In all cases, only those storms were selected for which concurrent solar wind and IMF data were available for the entire duration of the event. Interplanetary medium data were provided by Wind, ACE, and, to a lesser extent, by IMP 8 and Geotail. The inner magnetospheric field was represented using the newly developed T01 model [*Tsyganenko*, 2002a, 2002b], with a duskside partial ring current with variable amplitude and scale size, an essential part of the storm-time current system. The modeling revealed an enormous distortion and dawn-dusk asymmetry of the inner magnetosphere during the peak of the storm main phase, caused by the combined effect of the symmetric and partial ring currents, cross-tail current, and Birkeland currents. We found that during storms with Dst $<$ −250 nT the tail-like deformation of the nightside field penetrates so close to Earth that the quasi-dipolar approximation breaks down at distances as small as $3-4\ R_E$. This finding yields a quantitative answer to the question of why the auroras expand to unusually low latitudes during extremely strong storms. It also may provide a natural explanation for the observed impulsive injections and energizations of charged particles on the innermost L-shells. Finally, it questions the validity of using the dipole or quasi-dipole approximation in numerical simulations of severe storms in the inner magnetosphere.   INDEX TERMS: 2730 Magnetospheric Physics: Magnetosphere—inner; 2740 Magnetospheric Physics: Magnetospheric configuration and dynamics; 2708 Magnetospheric Physics: Current systems (2409); 2753 Magnetospheric Physics: Numerical modeling; 2778 Magnetospheric Physics: Ring current; KEYWORDS: inner magnetosphere, space storms, geomagnetic field, empirical modeling, partial ring current, field line deformation

1.   Introduction

[2]   Large magnetospheric disturbances have always been central to Sun-Earth connection studies. They are undoubtedly among the most interesting phenomena in space

physics and also a core subject of space weather, owing to their dramatic impact on the upper atmosphere, ionosphere, and the inner magnetosphere. Modeling the effects of major storms is quite important from both theoretical and practical viewpoints.

[3] This paper deals with the modeling of geomagnetic effects of strong storms in the inner and near magnetosphere, based on large sets of spacecraft data. Major magnetospheric storms are relatively rare events: as in the case of Earth's atmospheric storms, earthquakes, solar flares, etc., the occurrence frequency of geomagnetic disturbances rapidly decreases as their magnitude grows. Thus stormy periods with Dst < −100 nT comprise no more than a few percent of the total spacecraft and ground observations.

[4] Data-based models derived from space magnetometer experiments have been widely used in many studies where a field line mapping was required between low altitudes and the distant magnetosphere. However, all existing models of that kind used data sets, in which storm-time observations were diluted by much larger amounts of quiet-time data. Therefore using those models for mapping a strongly disturbed geomagnetic field is, in fact, an extrapolation, whose accuracy is questionable and hard to verify.

[5] Another limitation of the empirical approach is the way they have used the external input from the solar wind. Magnetospheric storms are dynamical events, in which not only the current state of the interplanetary medium is important but also its time history during the previous 1−3 hours. In this regard, different parts of the magnetospheric current system have largely different relaxation and inertia time scales. In most of the existing models these effects have been neglected, and the driving effect of the solar wind was assumed only as a function of the current state of the solar wind and the interplanetary magnetic field (IMF). The first attempt to overcome that limitation was made in a recent work [Tsyganenko, 2002a, 2002b; hereinafter referred to as T02a, b], where the strengths of the tail, Birkeland, and partial ring currents at any given time included terms with the factors G_1 and G_2, defined as integrals of geoeffective IMF-related parameters over the preceding 1-hour interval.

[6] There is sound theoretical and experimental evidence of a nonlinear response of the magnetosphere to abnormally strong disturbances in the solar wind. In early works [Reiff et al., 1981; Reiff and Luhmann, 1986] it was shown that the cross-polar potential saturates during the periods with very large southward IMF. Recent MHD simulations [Raeder et al., 2001] also have revealed significant saturation effects. There is little doubt that to a greater or lesser degree, all magnetospheric current systems respond nonlinearly to extremal conditions in the solar wind. Existing empirical models do not properly take this into account. For example, in the T96 model [Tsyganenko, 1995, 1996] the magnitude of the cross-tail current was assumed to be a linear combination of an IMF-related factor and of the square root of the solar wind ram pressure. However, no attempt was made to experiment with other possible combinations of the solar wind and IMF parameters, nor were the limits of validity of the linear approximation accurately evaluated, mainly because of an overwhelming predominance of the quiet-time data.

[7] The purpose of this work is to fill in that gap by developing an empirical model of a strongly disturbed

magnetosphere based on a new set of data comprising 37 storms during the period 1996–2000. To properly represent the storm-time changes of the magnetospheric magnetic field, one needs full information on the external input for the entire duration of the events included in the database, as well as a physically meaningful method to relate that input to the model parameters. Accordingly, in the following sections we describe in detail the data set and the way of parameterizing the model by the available solar wind characteristics. The adopted model approximation of the geomagnetic field is essentially similar to that described in T02a, and the reader is referred to that paper for more details. To illustrate the severity of the distortion of the inner magnetosphere in the course of very large disturbances, we use the new model to analyze geomagnetic configurations during two events of extremely strong space storms with Dst ≤ −250 nT.

2. Data

[8] Table 1 shows a list of all 37 events chosen for the modeling data set. Only storms with peak Dst lower than −65 nT were selected for this study. We also required that the entire interval of a storm be covered by concurrent solar wind and IMF data. Thanks to almost continuous monitoring of the solar wind by Wind (as well as by ACE in 1998–2000), in many cases complemented by simultaneous data from Geotail and IMP 8, that requirement was met in all the selected events. Occasional short gaps in the solar wind data were still allowed, and they were filled by interpolating the interplanetary parameters between their values at the edges of the gap. In total the relative duration of the gaps was less than 2% of the entire period of time covered by the 37 storms, and nearly half of them did not last longer than 5 min (i.e., a single missing data record). The continuity of the solar wind and IMF data was needed for the calculation of the external input indices for any given time moment during a storm.

[9] It was also required that magnetometer data from at least one spacecraft inside the inner/near magnetosphere were available for the storm period. However, unlike in the case of the solar wind data, we did not require that the magnetospheric magnetic field data be continuous throughout a storm.

2.1. Magnetospheric Magnetic Field Data

[10] The magnetospheric magnetic field data set comprised a total of 142,787 5-min average vectors. Owing to virtually continuous coverage of the concurrent variation of the magnetic field at geosynchronous orbit by GOES and in a wide range of latitudes by Polar, we were able to derive the response of main magnetospheric current systems to the external drivers. Figure 1 shows the spatial coverage of the inner magnetosphere by the data, projected into the GSM equatorial and noon-midnight meridian planes.

[11] Each dot in the plot corresponds to a 5-min average data record in the data set. The largest amount of data were contributed by GOES-8 (4171 hours), followed by Polar (3813), GOES-10 (1752), GOES-9 (1703), Geotail (775), and Equator-S (138). In general the procedure of preparing the data was similar to that described in T02b; it included removal of data records corresponding to magnetosheath or

Table 1. List of Storms and Spacecraft That Contributed in the Modeling Data Set[a]

Storm Dates	Year	min Dst	Magnetosphere Data	Interplanetary Data
22–26 Oct [*]	1996	−122	POL, G8, G9	WIND
10–15 Jan [*]	1997	−84	POL, G8, G9	WIND
10–12 Apr	1997	−91	POL, G8, G9	WIND, GTL
21–25 Apr	1997	−100	POL, G8, G9	WIND, GTL, IMP8
1–4 May	1997	−80	POL, GTL, G8, G9	WIND, GTL, IMP8
15–18 May	1997	−125	POL, G8, G9	WIND, GTL, IMP8
26–29 May	1997	−85	POL, GTL, G8, G9	WIND, GTL, IMP8
3–6 Sep [*]	1997	−99	POL, GTL, G8, G9	WIND, GTL, IMP8
8–14 Oct [*]	1997	−139	POL, GTL, G8, G9	WIND, GTL, IMP8
5–12 Nov [*]	1997	−124	POL, GTL, G8, G9	WIND, GTL, IMP8
22–25 Nov	1997	−121	POL, G8, G9	WIND
17–21 Feb [*]	1998	−119	POL, G8, G9, EqS	WIND, ACE
10–17 Mar [*]	1998	−118	POL, G8, G9, EqS	WIND, ACE, IMP8
2–7 May [*]	1998	−264	POL, G8, G9, GTL	WIND, ACE, GTL
6–10 Aug [*]	1998	−169	POL, G8, GTL	WIND, ACE, GTL, IMP8
26 Aug–3 Sep [*]	1998	−172	POL, G8, GTL	WIND, ACE, GTL, IMP8
24–28 Sep	1998	−213	POL, G8	WIND, ACE, GTL, IMP8
19–23 Oct [*]	1998	−119	POL, G8, GTL	WIND, ACE, GTL, IMP8
5–11 Nov [*]	1998	−179	POL, G8, GTL	WIND, ACE, GTL
13–16 Nov	1998	−123	POL, G8, GTL	WIND, ACE, GTL, IMP8
17–21 Feb	1999	−128	POL, GTL	WIND, ACE
28 Feb–5 Mar	1999	−93	POL, GTL	WIND, ACE
16–18 Apr	1999	−123	POL, G8, G10	WIND, ACE, IMP8
22–25 Sep	1999	−161	POL, G8, G10	WIND, ACE, GTL, IMP8
21–25 Oct [*]	1999	−223	POL, GTL, G8, G10	WIND, ACE, GTL, IMP8
11–16 Feb [*]	2000	−164	POL, G8, G10	WIND, ACE, IMP8
6–12 Apr	2000	−318	G8, G10	WIND, ACE, GTL
15–18 Apr	2000	−93	GTL, G8, G10	WIND, ACE, IMP8
24–26 Apr	2000	−78	GTL, G8, G10	WIND, ACE, IMP8
15–18 Jul	2000	−338	POL, G8, G10	WIND, ACE, GTL
19–24 Jul	2000	−96	POL, G8, G10	WIND, ACE, GTL
10–15 Aug	2000	−234	POL, G8, G10	WIND, ACE, GTL
12–14 Sep	2000	−66	POL, G8, G10	WIND, ACE, GTL
15–21 Sep	2000	−196	POL, G8, G10	WIND, ACE, GTL
2–8 Oct	2000	−184	POL, GTL, G8, G10	WIND, ACE, GTL
13–16 Oct	2000	−100	POL, G8, G10	WIND, ACE, GTL
4–8 Nov [*]	2000	−174	POL, GTL, G8, G10	WIND, ACE, GTL

[a]Asterisks denote the events comprising the Subset I (see text). POL - Polar; G8, G9, G10 - GOES 8, 9, 10; GTL - Geotail; EqS - Equator-S.
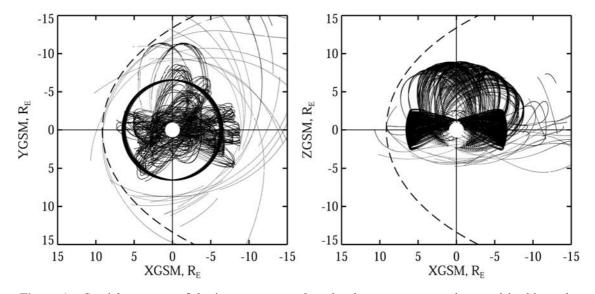

Figure 1. Spatial coverage of the inner magnetosphere by the magnetometer data used in this study, shown in the equatorial (left) and noon-midnight meridional (right) projections. Circular orbits of GOES spacecraft (a dense ring in the left panel), elliptical orbits of Polar with apogees at 8.8 R_E, and a few higher-apogee orbits of Equator-S are clearly visible. More sparse orbits of Geotail are also seen, located beyond $R \sim 10 R_E$. An average magnetopause position is shown by the broken line.

solar wind periods, subtraction of the Earth's main field, and averaging over 5-min intervals.

[12]   In some cases a correction of systematic errors in the data was made. One of them concerned a systematic small shift in the Geotail B_z component; that correction was described in more detail in T02b and will not be discussed here. It was also found that the data of GOES-8 contained a systematic offset in the H component, parallel to Earth's rotation axis. The existence of the offset was prompted by a comparison of GOES-8 magnetic field data with the output of T96 model (J. K. Chao, private communication, 2001), which indicated systematically lower fields in the subsolar region of the geosynchronous orbit. To carefully evaluate the actual magnitude of the offset, we performed a comparison of GOES-8 data with those of Polar and two other GOES spacecraft, as detailed below.

[13]   The direct comparison of the magnetometer data of GOES and Polar was possible due to several close conjunctions of the spacecraft in 2000. By that time, the apsidal precession of Polar's orbit brought its apogee to lower latitudes in the Northern Hemisphere so that the outbound legs of the spacecraft trajectory passed close to geosynchronous orbit. We searched for close conjunctions of the GOES-8 and -10 spacecraft with Polar in 2000 and found 9 and 11 cases, respectively, in which the spacecraft were separated by less than $\Delta R = 0.5\ R_E$. Since the distance ΔR between the two spacecraft during a conjunction remains finite (though quite small), a part of the difference between the observed fields is due to the spatial inhomogeneity of the geomagnetic field. At geosynchronous orbit the main contribution to the quiet-time field gradient comes from Earth's internal sources so that the spatial variation of B_z between Polar and GOES-8 can be reduced by subtracting the IGRF model field from the observed one.

[14]   The scatter plots in Figure 2 compare the 5-min average values of B_z (in GSM coordinates, after subtracting the IGRF field), observed during the conjunctions of GOES-8 (left) and GOES-10 (right) with Polar. Values obtained from Polar and GOES data are plotted along the horizontal and vertical axes, respectively. It is clearly seen that the GOES-8 data are shifted upward from the main diagonal, whereas GOES-10 observations are much closer to those of Polar. Equations of the best-fit linear regression lines in the plots provide the numerical values of the B_z offsets for GOES-8 and -10, equal to 7.22 nT and 1.04 nT, respectively.

[15]   Similar plots were generated for B_x and B_y components. Even though they showed much larger scatter than in the case of B_z (due to highly structured sheet-like azimuthal currents in the equatorial region), no significant offsets were found for those components.

[16]   A significant limitation of the above method is the lack of Polar-GOES conjunctions for earlier years so that we could not check the offsets for 1996–1999. Likewise, in 2001 there were only two conjunctions with $\Delta R \leq 0.5\ R_E$, owing to the further shift of the Polar apogee towards the equatorial plane.

[17]   The above finding was confirmed using an independent method based on the intercomparison of GOES-8 data with those from GOES-9 and -10. It allowed us to evaluate the offset for the entire period 1996–2000. The approach was to calculate the annual averages of the measured B_z for
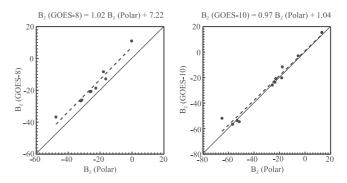

Figure 2.   Comparison of the measured values of B_z (external part only) during conjunctions of GOES-8 (left) and GOES-10 (right) with Polar in 2000. Linear regression fits are shown by broken lines, and the corresponding equations are given above the plots.

each of 24 one-hour intervals of the magnetic local time (MLT), using concurrent data of GOES-8 and GOES-9 (or GOES-10). The method takes advantage of the fact that beginning from 1996, the geosynchronous magnetic field was measured simultaneously by two spacecraft, separated by only 4 hours of local time. It means that each of the 24 MLT sectors was sampled twice a day: first by GOES-8 and then (4 hours later) by GOES-9 (in 1996, 1997, and 1998) or by GOES-10 (from 1999 on). We use here only quiet-time data with $|\mathrm{Dst}| \leq 15$ nT, to minimize possible temporal changes of the magnetic field during the 4-hour interval between the successive sampling of a given MLT sector by GOES-8 and the trailing spacecraft. Since the contribution of the Earth's main field was removed from the data, the only remaining source of the systematic shift of B_z (other than the instrumental offset) could be the difference between the values of the dipole tilt angle, corresponding to the 4-hour lag in the universal time. The tilt angle affects the geometry of external currents, and hence its changes contribute to the variations of the geosynchronous field within a fixed MLT sector. That effect can be easily evaluated using the quiet-time output of a suitable data-based model in place of the GOES data. Using the latest model of the inner magnetospheric field [T02a, b], we found that the expected average diurnal variation at the GOES-8 location had a slightly larger peak-to-peak amplitude, with the noon maximum and midnight minimum equal to 17.0 nT and −26.5 nT, respectively, as compared with that at GOES-10 location, where the model B_z varied between 13.5 and −24.4 nT. However, no significant shift was found between the model B_z variations at GOES-8 and -10 locations.

[18]   Let us now turn to the observed average diurnal variations. Figure 3 compares annual average diurnal variations of the external B_z (GSM) at GOES-8 and two other synchronous spacecraft for 6 years since 1996. Rms deviations (shown by vertical bars) in all cases varied from 5 to 10 nT. A significant positive shift of GOES-8 data can be clearly seen in all six panels, with annual averages for different years varying between 6.0 and 6.5 nT, in good agreement with the independent test based on GOES-Polar conjunctions (Figure 2). Since the attitude of the GOES-8 spacecraft was actually stabilized with respect to Earth's frame of reference, we also made a similar calculation,
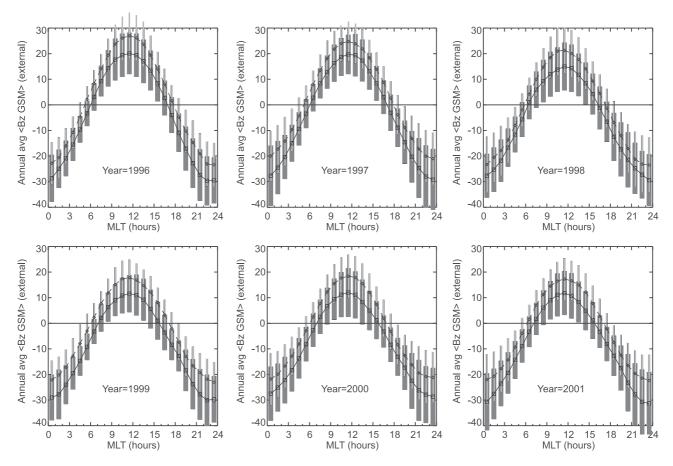
Figure 3. Annual average diurnal variation of B_z (GSM) as observed by GOES-8 (broken curves) compared with that of GOES-9 (solid curves, top row) and GOES-10 (solid curves, bottom row). Rms deviations are also shown for each MLT hour (GOES-8: light thin bars, GOES-9, -10: dark thick bars).

using the geographic (GEO) coordinate system instead of the GSM. The resultant offset was found to be slightly larger in that case, equal to 7.0 nT, and that value was used for correcting all GOES-8 data used in this study.

2.2. Interplanetary Medium Data

[19] For each event in our 37-storm set we produced a continuous record of the interplanetary conditions. These records were derived from the individual spacecraft data, reduced to Earth's location using concurrent values of the observed flow speed and the X-coordinate of the monitoring spacecraft. In general the procedure was as follows. The entire storm period (covering typically from 3 to 10 days) was divided into a sequence of 5-min intervals. In the simplest case when, for a given 5-min interval, the solar wind/IMF data were available from only one spacecraft, those data were adopted without any changes. In cases of more than one contributing spacecraft, a weighted averaging was made, based on such factors as positions of the monitors with respect to the Sun-Earth line and the magnetosphere, noise level in the data, and others. For example, if the data from WIND and ACE were available for a given interval, with both spacecraft near the L1 point, then their weights were assumed equal. If WIND was located closer to Earth and not too far from the Sun-Earth line (within 50 R_E), its data were preferred over those of ACE. In some cases, the only available interplanetary medium data were those from

Geotail, which periodically entered in the solar wind during the spring, summer, and fall seasons. While most of Geotail's IMF and solar wind speed observations showed a good agreement with those of other spacecraft, its proton density data often exhibited large abnormal excursions, presumably due to foreshock effects [e.g., *Sibeck et al.*, 2001]. Similar anomalies were also observed in some of the IMP 8 data. For that reason the Geotail and IMP 8 solar wind data were used with caution and only in the absence of WIND and ACE data.

[20] To accurately evaluate the solar wind ram pressure, one needs not only the proton density but also that of the alpha-particles, the second major ion species of the solar wind. In the initial calculations the relative number density N_α/N_p of the alpha-particles to protons was assumed either equal to its average value of 4% (for 1996 and 1997) or was taken from the ACE key parameter data (for 1998 and later years). In the final version of our storm database we used the values of N_α/N_p from the WIND solar wind plasma experiment.

[21] In terms of the temporal variation of the main interplanetary parameters which drive storms, individual events in our collection represent many different scenarios. Figures 4–7 display some examples of the storms from Table 1. The upper panel in each figure shows the variation of the Dst index from the beginning to the end of a storm. The subsequent four panels (from top downward) display the behavior of the B_y and B_z GSM components of the IMF, and
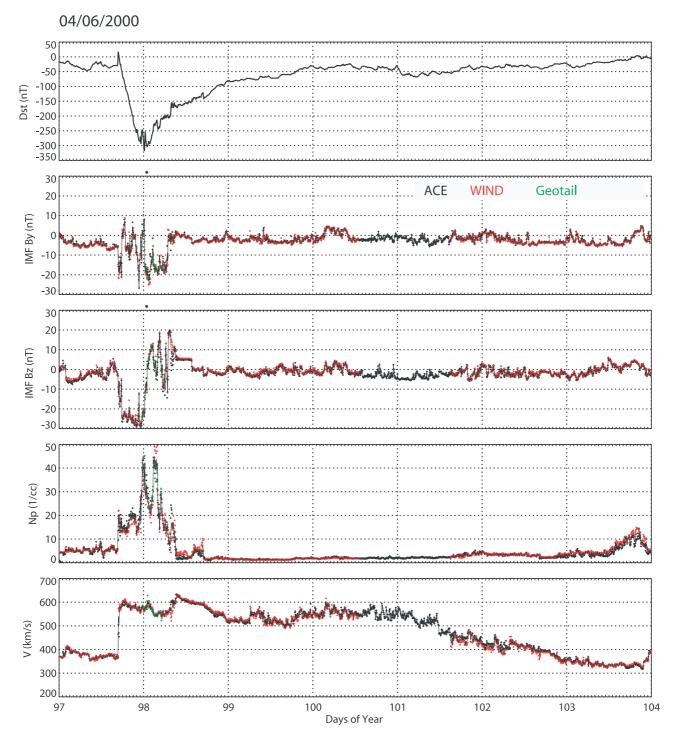
04/06/2000

Figure 4.   Dst-index, solar wind, and IMF parameters during the storm of 6−12 April 2000.

the solar wind proton density and bulk flow speed, as observed by different spacecraft in the solar wind. The origin of the solar wind/IMF data is coded by the colors of the dots, according to the legend in the second panel. Each dot represents a 5-min average of an interplanetary parameter. The thin solid line in each panel shows the final continuous approximation for each of the four interplanetary parameters.

[22]   Figure 4 shows the major storm of 6−12 April 2000. This is a classic example, with a minor disturbance in the morning of the first day, caused by a negative excursion of the IMF B_z, a brief sudden commencement at 1645 UT due to the arrival of a shock front, followed by a steady decrease of the Dst index down to −300 nT, and a gradual recovery during the next few days.

[23]   Figure 5 (the storm of 21−25 October 1999) is another example of storm development. Here the initial rapid decrease of Dst in the first two hours of October 22 temporarily slows down, due to the temporary recovery of the IMF B_z from −20 to −10 nT, and then resumes, in response to a further drop of the IMF B_z down to −30 nT.
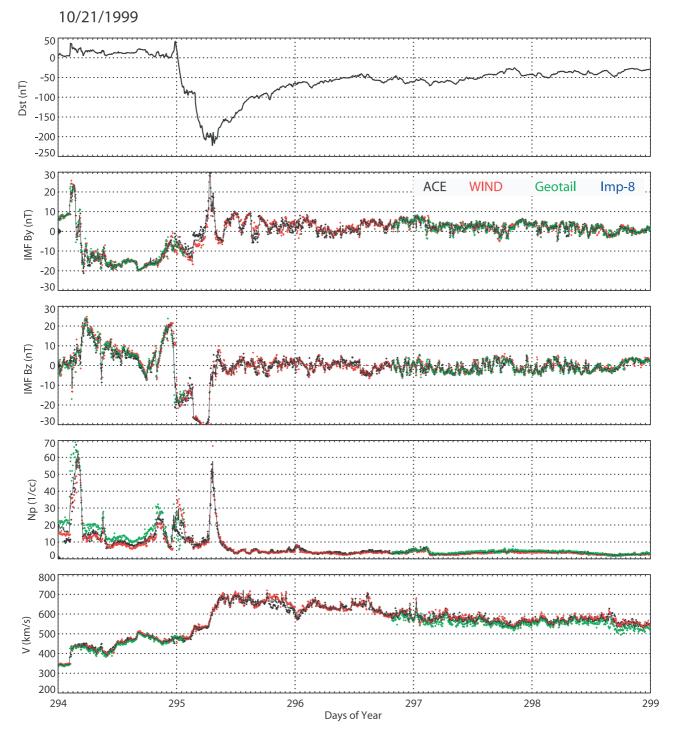
Figure 5. Dst-index, solar wind, and IMF parameters during the storm of 21–25 October 1999.

[24] The next example, in Figure 6, is the well-known Bastille Day storm of 15 July 2000. The solar wind plasma data for the first day of this storm were provided by Geotail, which fortunately was in the solar wind at that time, while ACE plasma data were unavailable for that period. The recovery phase (16–18 July) was well covered by the ACE solar wind plasma observations. The IMF data for the entire period were provided by WIND magnetometer (courtesy of A. Szabo).

[25] Figure 7 shows an interesting example of a relatively weak disturbance of 16–18 April 1999, with Dst $\sim$ −120 nT

at the peak of the main phase. It was caused by a transient magnetic cloud with a region of very high ($\sim$80 cm^{-3}) solar wind density at the leading edge and a roughly linear variation of the IMF B_z from −12 nT to +10 nT during the second day (17 April).

3. Model Magnetic Field Sources and Their Parameterization

[26] The magnetic field model used in this study was based on the recently developed approximations [T02a, b] for the
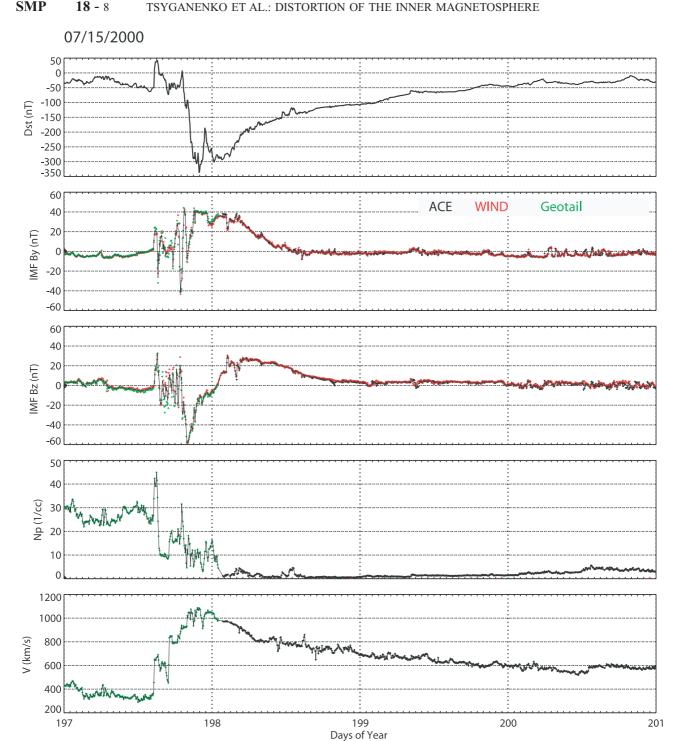
07/15/2000

Figure 6. Dst-index, solar wind, and IMF parameters during the storm of 15–17 July 2000.

main components of the magnetospheric field. In this work we give only a brief description of that model, and the reader is referred to the above cited papers for details. More attention will be given here to the parameterization of the field sources, since it includes some essentially new elements.

3.1. Principal Sources of the Model Field

[27] The model magnetopause was approximated by an ellipsoido-cylindrical composite surface, whose shape was fitted to the average boundary of *Shue et al.* [1998]. The size of the magnetopause was allowed to vary in response to the varying ram pressure P_d of the solar wind, in accordance with a simple self-similar scaling relation with a scaling factor $\chi = (P_d/P_{d0})^{\kappa}$, where P_{d0} is a reference average value of the pressure. The power index κ was allowed to vary, and its best-fit values in all runs were close to the theoretical estimate of 1/6. The second factor, affecting the shapes of the magnetopause and of the cross-tail current sheet, was the Earth's dipole tilt angle Ψ, entering as a parameter in a tilt-related deformation of the model field.
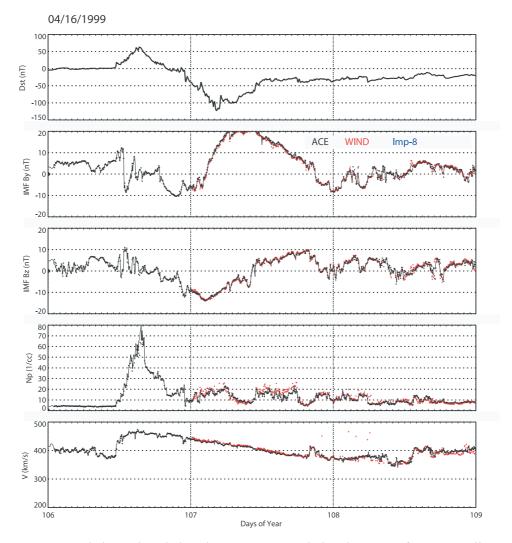
04/16/1999

Figure 7.   Dst-index, solar wind, and IMF parameters during the storm of 16–18 April 1999.

[28]   The model included a scalable ring current, comprising its symmetric and partial components. The partial ring current (PRC) included a westward azimuthal current at low latitudes, closed via field-aligned currents and localized in the evening-premidnight sector. This component is quite important in the modeling of the disturbed inner magnetosphere since it provides the observed strong dawn-dusk asymmetry of the geomagnetic field, extending over a wide range of altitudes from geosynchronous orbit down to Earth's surface.

[29]   The magnetic field of the cross-tail current was represented by two modules with different scales of the radial variation of the electric current density so that the model field was sufficiently flexible to fit widely different observed radial profiles. The cross-tail current had several geometrical parameters, controlling its thickness, flankward expansion rate, tilt-dependent deformation, and variable shift along the tail's axis. Some of those parameters were kept fixed in the fitting runs because of a very limited data coverage at distances $R \geq 9-10\ R_E$. The tail field (as well as the field of other sources) was fully shielded inside the model boundary.

[30]   Contributions of the Region 1 and 2 field-aligned currents were represented by two separate modules, each of

which included two Fourier modes, to model variable local time profiles of the Birkeland currents. The global scale size of the field-aligned current circuits was represented as a function of the disturbance level (quantified by the 5-min average Dst/SYM-index), which made it possible to model the equatorward expansion and poleward contraction of the Region 1 and 2 ovals in the course of a storm.

[31]   Finally, the model included an interconnection field $\mathbf{B}_{int}$, representing the effect of the IMF penetration inside the magnetosphere. The interconnection term was modeled as a uniform field, whose magnitude was proportional to the transverse component $\mathbf{B}_\perp^{IMF}$ of the IMF, and its orientation followed the direction of $\mathbf{B}_\perp^{IMF}$. More details on the relation between $\mathbf{B}_{int}$ and $\mathbf{B}_\perp^{IMF}$ are given in the next section.

3.2.   Parametric Relations for the Model Field Sources

[32]   In general the parameterization scheme in this study is quite similar to that adopted in T02b. The difference here is that we concentrate exclusively on the inner magnetosphere (only ~3% of the data used in this study came from distances beyond $R = 10\ R_E$) during strongly disturbed periods. For these reasons a few terms have been omitted in the expansions for the model tail field, and nonlinear saturation effects have been taken into account. We briefly

reproduce below the adopted parametric expansions for the magnitude of the model field sources, paying most attention to the main differences from the earlier work.

[33] The tail amplitude coefficients t_1 and t_2 (for the short- and medium-scale modules, respectively), were assumed as

$$t_1 = t_1^{(0)} + t_1^{(1)}(P_d/P_{d0})^{\alpha_1} + t_1^{(2)}G_2/\sqrt{G_2^2 + G_{t1}^2} + t_1^{(3)}Dst*$$
$$t_2 = t_2^{(0)} + t_2^{(1)}(P_d/P_{d0})^{\alpha_2} \qquad (1)$$

where P_d is the ram pressure of the solar wind, $P_{d0} = 2$ nPa is its average value, $Dst* = 0.8\,Dst - 13\sqrt{P_d}$ is the corrected Dst-index, and $G_2 = \langle VB_s \rangle/200$ is a parameter (introduced in T02b), proportional to the hourly average of the solar wind speed V, multiplied by the southward component B_s of the IMF ($B_s = -B_z$ for $B_z < 0$ and $B_s = 0$ for $B_z \geq 0$). Here the averaging is made over the preceding 1-hour interval, and the normalization factor 1/200 brings the values of G_2 into a convenient range between 0 (quiet-time solar wind) and ~200 (an extremely strong dawn-dusk IEF of 40 mV/m). The coefficients $t_1^{(1)}$ and $t_2^{(1)}$, as well as the power indices α_1 and α_2 define the sensitivity of the tail field to variations of the solar wind ram pressure. Equation (1) differs from equation (2) of T02b in that here we omitted the Dst- and the IMF-related terms in the second module, used the parameter G_2 instead of G_1, and introduced a nonlinear dependence of the tail field on that parameter. The nonlinearity implies a gradual saturation of the cross-tail current for the values of G_2 exceeding a threshold G_{t1}, an interesting effect ignored in T02b. In this work we introduced the nonlinear saturation not only for the cross-tail current but also for the field-aligned and partial ring current sources.

[34] The need for taking into account the nonlinear saturation can be understood, for example, from a simple estimate of the magnitude of the Region 1 Birkeland currents in T02a, b, based on the observed range of values of the driving parameters G_1 and G_2. During quiet times, both G_1 and G_2 are close to zero; for moderately disturbed periods with IMF $B_z \sim -5$ nT they are on the order of 10; during larger storms with Dst ~ -120 nT they can reach values between 30 and 60, and during great space storms (like that on the Bastille Day of 2000) can well exceed 200. In the first case, using the linear approximation in equation (8) of T02b for the total Region 1 current (downward current per one hemisphere), $J_{\text{tot}} = 0.28 + 0.17\,G_2$ provides a reasonable value $J_{\text{tot}} \sim 2$ MA. In the second case, assuming $G_2 \sim 50$ yields a hardly plausible estimate $J_{\text{tot}} \sim 9$ MA, and in the extreme case of a great storm one obtains $J_{\text{tot}} \sim 20$–40 MA, which is obviously unrealistic. Inside the polar cap, a Birkeland current of such magnitude would produce a horizontal magnetic field of ~3,000–5,000 nT, whereas the actual disturbances observed inside the polar caps even during the largest storms do not exceed ~500–1000 nT.

[35] To ascertain the latter estimate, we inspected a set of ground magnetograms of the Thule observatory and analyzed magnetometer data of 22 passes of the low-altitude Ørsted spacecraft (see *Stauning and Primdahl* [2000] for a detailed description of the mission) during great storms of 22 October 1999, 6 April 2000, and 31 March 2001. In all

cases, peak-to-peak geomagnetic variations on the ground, as well as typical polar cap disturbances observed above the ionosphere, did not exceed ~700 nT. The largest excursions of the field components were detected by Ørsted when it traversed the Birkeland current sheets; in those cases peak-to-peak variations reached ~1500 nT but never exceeded 2000 nT. Adopting the nonlinear response of the model field sources to the IMF-related parameters, like that introduced in equation (1), makes it possible to reconcile the model output with these observations.

[36] The magnitude of the symmetrical component of the ring current (SRC) was assumed here in the same form as in T02b, controlled by the corrected Dst-index and the solar wind pressure

$$s = s^{(0)} + s^{(1)}Dst* + s^{(2)}\sqrt{P_d}, \qquad (2)$$

and its scale size was also a variable quantity, controlled by the disturbance level.

[37] The magnitude of the PRC was approximated somewhat differently than in T02b: instead of the linear dependence on the Dst-index, we introduced a nonlinear term with a new driving variable $G_3 = \langle NVB_s \rangle/2000$, based on solar wind input. Like G_2, the parameter G_3 was defined as an average over the preceding 1-hour interval of a product of the geoeffective solar wind characteristics, and it varies within nearly the same range of values. It differs from the parameter G_2 in that in addition to the solar wind speed V and southward component of the IMF B_s, G_3 also includes the solar wind particle density N. The idea behind replacing Dst with a function of G_3 stemmed from the fact that the rapid buildup of the partial ring current is a result of the strongly enhanced, directly driven convection from the tail, and it should also quickly recede during the recovery phase [*Liemohn et al.*, 2001]. This type of behavior is readily reproduced by the driving variable G_3, while the Dst-index can stay quite low for many hours after the storm main phase, due to the much more slowly decaying SRC. The final form of the PRC amplitude coefficient reads

$$p = p^{(0)} + p^{(1)}G_3/\sqrt{G_3^2 + G_p^2} \qquad (3)$$

The coefficients $b_{1,2}$ defining the strength of the Region 1 and 2 Birkeland currents were assumed to have the form

$$b_{1,2} = b_{1,2}^{(0)} + b_{1,2}^{(1)}G_2/\sqrt{G_2^2 + G_{b_{1,2}}^2}, \qquad (4)$$

similar to equation (3) but with the parameter G_2 instead of G_3. The saturation thresholds G_{t1}, G_p, and G_{b12} in equations (1), (3), and (4) were treated as variable parameters; results of their fitting to the data are discussed in the next section.

[38] The IMF penetration inside the magnetosphere was approximated in the same way as in T02b, $\mathbf{B}_{\text{int}} = \varepsilon \mathbf{B}_\perp^{\text{IMF}}$. The coefficient of proportionality between the upstream component of the IMF $\mathbf{B}_\perp^{\text{IMF}}$ and the interconnection field $\mathbf{B}_{\text{int}}$ was assumed as a simple binomial function of the IMF clock angle θ

$$\varepsilon = \varepsilon_0 + \varepsilon_1 \sin^2 \frac{\theta}{2} \qquad (5)$$

The coefficients ε_0 and ε_1 were also treated as free model parameters to be derived from the data.

4. Results

[39] The goal of this work was to quantitatively estimate the degree of the storm-time deformation of the inner magnetosphere. In this section we discuss the best-fit values of the coefficients, obtained on the basis of the entire 37-storm data set, evaluate an overall performance of the model, and present some mapping results which answer the question posed in the title of this paper.

[40] An important aspect in all studies of this kind is the degree of a model's reliability, including estimates of the uncertainties of the model parameters and their effect on the mapping accuracy. A simple way to roughly assess the uncertainties and to estimate the reproducibility of the data by the model is to divide the entire input data set into two parts of nearly equal size and compare the results of fitting the model to these independent subsets. This way of testing the model can be viewed as a variant of the so-called "bootstrap" approach [*Press et al.*, 1992, chapter 15]. To that end, we divided the entire 37-storm data collection (henceforth referred to as Set) into two independent subsets, containing 15 and 22 different storms, respectively, with approximately equal number of 5-min data records. The selection is specified in Table 1, where the storms that entered in the first group (15 storms) are marked by asterisks. In the following sections we will refer to these subsets as Subset I and Subset II, respectively.

4.1. Tail Field

[41] The values of the tail field parameters obtained using the entire Set were $t_1^{(0)} = -1.19$, $t_1^{(1)} = 1.32$, $t_1^{(2)} = 0.41$, $t_1^{(3)} = -0.076$, $t_2^{(0)} = -1.97$, $t_2^{(1)} = 5.69$. Similar runs, but made using the Subsets I and II, yielded significantly different values: $t_1^{(0)} = -1.57$, $t_1^{(1)} = 1.45$, $t_1^{(2)} = 0.27$, $t_1^{(3)} = -0.089$, $t_2^{(0)} = -2.27$, $t_2^{(1)} = 6.12$, for the Subset I, and $t_1^{(0)} = -0.82$, $t_1^{(1)} = 0.81$, $t_1^{(2)} = 0.55$, $t_1^{(3)} = -0.070$, $t_2^{(0)} = -3.05$, $t_2^{(1)} = 6.82$, for the Subset II. A closer scrutiny revealed that the difference in the coefficients was partly due to an interplay between the short- and medium-scale modules so that in both cases the total tail field contribution in the inner magnetosphere was not too different. The interplay between the tail field modules was due to the facts that (1) the tail contribution in the inner magnetosphere is mostly a fringe field, whose distribution in that region is quite similar for both modules, and (2) as already noted, the percentage of data in the tail (at $R > 10~R_E$) was quite low. The best-fit value of the saturation threshold for the tail field was found to be equal to $G_{t1} = 12 \pm 2$, where the uncertainty value is based on the results fitting runs using Subsets I and II.

4.2. Symmetric and Partial Ring Current

[42] The best-fit values of the SRC coefficients based on the entire Set were $s^{(0)} = 0.80$, $s^{(1)} = -0.026$, and $s^{(2)} = -0.44$. The respective values obtained from the Subsets were (0.74, −0.024, −0.39), and (0.96, −0.027, −0.52). While the first and third coefficients do not differ too much from those obtained in T02b, the second one (by the Dst-index) is roughly 50% larger than in that model.

A possible reason is that here we omitted a Dst-related term in the second tail field module, and that led the fitting algorithm to offset the lack of tail's contribution in the inner field by increasing the ring current sensitivity to Dst.

[43] The PRC coefficients derived from the Set are $p^{(0)} = 0.86$ and $p^{(1)} = 5.75$. The saturation threshold $G_p = 83$ so that the strength of the PRC remains a linear function of G_3 even during large storms, and the saturation effect shows up only under extreme conditions. Fitting to the Subsets yielded significantly different (by $\sim 20-30\%$) values of the PRC coefficients. Plotting the resultant amplitude coefficient p against G_3 revealed that the difference actually showed up only for large values of the driving parameter, $G_3 \geq \sim 60$, observed only during a few strongest storms, while for $G_3 \leq \sim 60$ the PRC magnitudes derived from Subsets I and II were quite close to each other (within $10\%-15\%$). The discrepancy was found to be due to largely different values of the saturation threshold G_p (equal to 35 and 440 for the 15- and 22-storm subsets). A closer inspection of the data revealed that Subset II, in contrast to Subset I, did not contain any data taken in the low-latitude dusk sector at $R \leq 4-5~R_E$ during major storms with $G_3 > 100$. It therefore could not provide any reliable information on the behavior of the partial ring current for extremal values of the driver G_3. The average local time position of the center of the PRC was also treated as a variable parameter, and its best-fit value was found equal to $\phi = 70 \pm 15°$ (magnetic longitude angle, measured from the midnight meridian duskward).

4.3. Region 1 and 2 Birkeland Currents

[44] The behavior of the model Region 1/2 Birkeland currents in response to the external parameter G_2 agreed reasonably with expectations. For the principal mode (varying as $\sin\phi$) of the Region 1 current system, the free term $b_1^{(0)}$, the coefficient $b_1^{(1)}$, and the saturation threshold G_{b1}, were equal to 0.46, 4.63, and 27.2, respectively. That yields the total downward Region 1 current of ~ 0.5 MA for purely northward IMF, ~ 2 MA for moderately disturbed conditions with $G_2 = 10$, and the saturation limit of ~ 5.1 MA for the extremal case of a very large southward IMF. For the second harmonic of the Region 1 current (proportional to $\sin 2\phi$) the corresponding best-fit parameters were found equal to 0.077, 1.38, and 98.4. Based on equation (4), these values imply that for low and moderate values of the parameter G_2 the Region 1 current peaks at dawn and dusk, while during strongly disturbed times the peaks shift towards noon.

[45] The Region 2 currents behave, generally, in the same manner as the Region 1, with the difference that their magnitude saturates at ~ 1.7 MA, i.e., nearly at 1/3 of the Region 1 upper limit, and, as expected, they have opposite polarity. Numerical values of their parameters are as follows: for the principal (sinusoidal) harmonic $b_2^{(0)} = -0.14$, $b_2^{(1)} = -1.6$, and $G_{b2} = 14.4$. The second harmonic has the following coefficients: $b_2^{(0)} = 0.11$, $b_2^{(1)} = -0.14$, $G_{b2} = 4.8$, and hence it remains relatively small for all values of the parameter G_2. One should have in mind that in terms of the physics, the storm-time Region 2 currents can be viewed as the outer part of the PRC, represented in our model as a
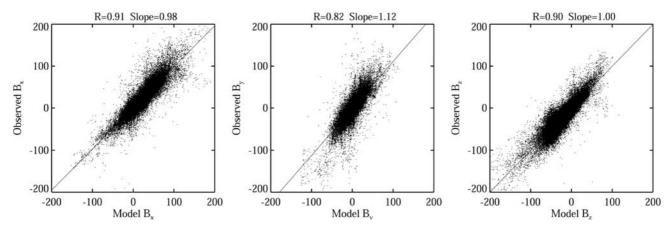
Figure 8. Scatter plots of the observed values of the external magnetic field components against those returned by the model.

separate current system. A more detailed discussion of that question was given in T02.

4.4. IMF Interconnection Field

[46] The penetration coefficient ε_0 for the IMF interconnection field was found equal to 0.42 ± 0.02. The modulation by the IMF clock angle, quantified by the second term in equation (5), was found relatively small, with the coefficient $\varepsilon_1 = 0.08 \pm 0.03$. This is quite different from what was found in T02b: in that model the free term was relatively small and the efficiency of the penetration greatly increased during southward IMF conditions. However, the average degrees of the southward IMF penetration (~ 0.5) are roughly the same in both models.

4.5. Overall Approximation Quality

[47] Similarly to T02, the overall performance of the model approximation was evaluated by statistically comparing the observed and predicted values of the external (i.e., without Earth's contribution) magnetic field components. Figure 8 displays scatter plots of the values of three GSM components of the observed external field, against those returned by the model. The plots include all 142,787 data records used in the fitting of the model by least squares. The corresponding correlation coefficients R and the slopes of the best linear fit to the scatter plots are shown in the top of each panel. As in T02, the largest correlation coefficient $R = 0.91$ was found between the observed and model values of the B_x component, in part due to its large and well-ordered variation across the equatorial current sheet on the nightside. For the B_z component the overall correlation is a little lower, $R = 0.90$, and there is a distinct increase of the data scatter around the best-fit line from positive to negative values of B_z. This indicates a larger scatter of B_z on the nightside, associated with spontaneous substorm dipolarizations. The lowest correlation (0.82) was found for B_y component; however, it is much better than in T02, where B_y yielded the correlation coefficient of only 0.67.

5. Mapping Results and Discussion

[48] One of main goals of this work was to evaluate the degree of the distortion of the inner geomagnetic field during strong space storms. Principal electric current systems that contribute to that distortion are the symmetrical

and partial ring current, as well as the near part of the tail current. In our model these sources are controlled by the Dst-index, IMF-related variables G_2 and G_3, and the dynamic pressure P_d of the solar wind. Based on this, one should expect that the strength of the magnetospheric currents (and hence the field distortion) peaks some time during the main phase of a storm, when the effect of large and prolonged southward IMF, combined with high-speed and dense solar wind reaches its maximum, and manifests itself in large negative values of both *Dst* and *dDst/dt*.

[49] Figure 9 shows a noon-midnight plot of the model field lines, corresponding to the end of the main phase of the storm of 6 April 2000. In this case the input model parameters corresponded to UT = 2200 of Day 97 (04/06/00): Dst = −250 nT, IMF B_y = −7.9 nT, B_z = −28.6 nT, G_2 = 77, G_3 = 145, and the dipole tilt angle Ψ = 8.9°. The most striking
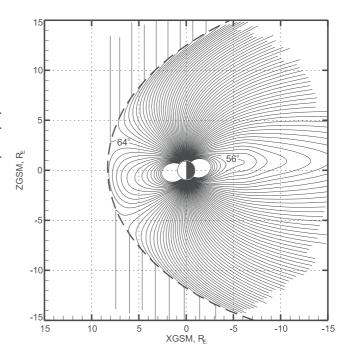

Figure 9. Noon-midnight configuration of the model geomagnetic field lines, corresponding to stormy conditions at UT = 2200 of 6 April 2000. The lines are plotted every 1° in footpoint magnetic latitude, beginning with 50°.
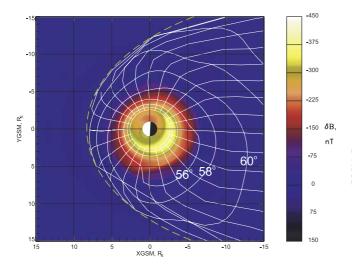
Figure 10. Contours of constant magnetic latitude (at 2° intervals) and constant local time (at 1-hour intervals) at the Earth's surface as mapped along model field lines to the equatorial plane, for the same set of model parameters as in Figure 9, corresponding to UT = 2200 of 6 April 2000. The background color displays the equatorial distribution of the difference δB between the magnitudes of the total model field and the purely dipolar one.

Figure 11. Same as Figure 9 but for UT = 0800 of 31 March 2001.

feature is an enormous stretching of the field lines on the nightside so that the line with a footpoint magnetic latitude of 56° normally residing deep in the inner magnetosphere ($L \sim 3.2$) becomes swept to the synchronous distance, $6-7\ R_E$.

[50] In this regard an important question still remains open, whether the higher-latitude tail field lines are actually open or closed across the current sheet within $R \leq 15\ R_E$, as implied by the model mapping in Figure 9. As clearly seen in Figure 1, the data coverage of the near tail is greatly reduced at distances $R > 8.8\ R_E$ beyond the apogee of Polar. In addition the variability of the model tail field structure and its sensitivity to the external input dramatically rises with the growing distance. For that reason, one should not rule out that the field lines with footpoint latitudes above $55-56°$ can at times map much farther tailward or even become open. The severe stretching of the inner magnetic field lines, demonstrated by our modeling study, quantitatively explains the dramatic equatorward expansion of the equatorward boundary of the auroral oval during major space storm events.

[51] Another noteworthy feature is the very low latitude, ∼64°, of the polar cusp footpoint. It manifests the overall equatorward expansion of the auroral oval (and the associated increase of the polar cap magnetic flux), and agrees quite well with existing case studies of the polar cusp storm-time dynamics [e.g., *Meng*, 1983].

[52] Figure 10 illustrates the global mapping of the inner magnetospheric field lines at all local times, corresponding to the same case as in Figure 9. It displays the lines of constant magnetic latitudes and MLT, mapped from the ground to the equatorial plane. The background color indicates the distribution of the scalar difference δB between the magnitudes of the total model field and that due to Earth's internal sources. Red and yellow colors correspond to the region of a strong near-Earth depression, owing to the partial and symmetrical ring currents. The most conspicuous
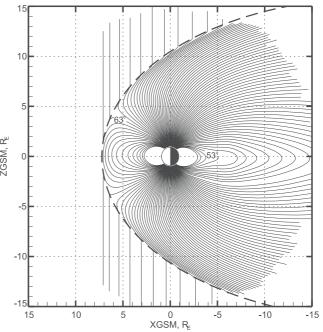
feature is the remarkable dawn-dusk asymmetry with a much deeper depression in the dusk-premidnight sector. The asymmetry is due to the PRC, and one clearly sees that the enhanced depression on the duskside extends from high altitudes $(3-4\ R_E)$ all the way to the ground. This is in line with ground-based observations of the storm-time asymmetry of the Dst-field and is due to the field-aligned currents, closing the PRC via the ionosphere. The asymmetry in the δB distribution is clearly matched by that in the shape of the nested contours of the mapped magnetic latitudes, with a conspicuous bulge on the duskside.

[53] Figures 11 and 12, similar in their format to Figures 9 and 10, illustrate the mapping for an outstanding space storm event of 31 March 2001 (not included in the modeling
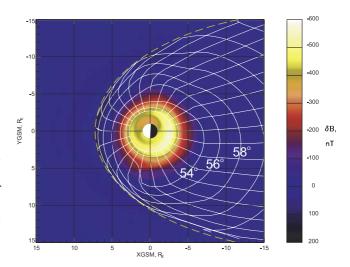

Figure 12. Same as Figure 10 but for UT = 0800 of 31 March 2001.

data set), accompanied by a significantly larger magnetospheric distortion. In this case, at UT = 0800, the nightside field lines with footpoints as low as 53° ($L \sim 2.8$ under normal conditions) were stretched to 5 R_E, where the field became essentially tail-like. At that time, the Dst-index (SYM) reached −410 nT, with P_d = 17.9 nPa, IMF B_z = −33 nT, G_2 = 126, G_3 = 252, and the dipole tilt was −2°. The concurrent magnetic latitude of the dayside cusp footpoint was only 63°.

[54] The model can be checked for its consistency with the ground data by comparing the actually observed Dst-index with the predicted ground depression, averaged over the magnetic local time. In the first example of the storm of 6 April 2000, the actual Dst (SYM) at UT = 2200 was −250 nT, while the total MLT-averaged contribution from the external sources was −268 nT, reasonably close to the observed one. In the second example (31 March 2001, 0800 UT), the agreement appears even better: the observed Dst was −410 nT, while according to the model the average ground depression was −416 nT. Note however that in the above comparison we did not include the effect of the induction currents, which could significantly (up to ∼30%) increase the estimate of the ground magnetic field depression and thus worsen the agreement.

[55] One of possible sources of that discrepancy is the geocentric closure of the field-aligned currents, assumed in T02. That assumption greatly simplified the calculation by making it possible to use a simple deformed conical current sheet model. It virtually did not affect the model field beyond $R \sim 2\ R_E$ but could have resulted in a gross disagreement with observations below the ionosphere. In general, reconciling the ground-based and space observations of the disturbed geomagnetic field and constructing a comprehensive unified field model is still a largely unsolved problem. A detailed treatment of this subject extends beyond the scope of this paper and will not be pursued here.

[56] Another interesting question is the relative magnitude of contributions to the total ground disturbance of the geomagnetic field from the individual magnetospheric sources. Here we confine our analysis to only the equatorial magnetic field. In the first of the above two examples (6 April 2000, 2200 UT), the values of contributions to the total equatorial B_z (in GSM coordinates), averaged over all local times, are as follows: (1) Chapman-Ferraro currents (dipole shielding field only), $B_z^{(CF)}$ = 33 nT, (2) the shielded cross-tail current system, $B_z^{(T)}$ = −119 nT, (3) symmetrical ring current, $B_z^{(SRC)}$ = −152 nT, (4) partial ring current, $B_z^{(PRC)}$ = −20 nT, (5) Region 1 field-aligned current, $B_z^{(R1)}$ = −13 nT, (6) Region 2 field-aligned current, $B_z^{(R2)}$ = 17 nT, (7) IMF interconnection field, $B_z^{(int)}$ = −14 nT. As can be seen, the largest negative contributions come from the SRC (−152 nT) and from the cross-tail current (−119 nT). The contributions from the field-aligned currents and the PRC at noon and midnight have actually the same order of magnitude. However, since they vary with the local time between large positive and negative peak values, their MLT averages are relatively small.

6. Conclusions

[57] We presented here first results of the data-based modeling of the stormy magnetosphere, using a new collection of space magnetometer data, taken in the inner magnetosphere during 37 major disturbances in 1996–2000. All the events were covered by concurrent solar wind and IMF data, and their magnitude ranged between Dst = −66 nT and Dst = −338 nT. The magnetic field model was based on the most recent work [T02a] and included flexible representations for all major field sources, in particular a scalable ring current, with a partial component centered in the evening MLT sector and providing a strong dawn-dusk asymmetry of the disturbed geomagnetic field. The strengths of the cross-tail current, the partial ring current, and the field-aligned currents were parameterized using interplanetary indices G_2 and G_3, taking into account both time-integration effects and a nonlinear saturation of the magnitude of the magnetospheric sources during periods of extreme IMF and solar wind conditions.

[58] One of the goals of this work was to quantitatively estimate the degree of the storm-time distortion of the inner magnetosphere during major space storms. Applying the model to the 6 April 2000 event has shown that the outward stretch of the geomagnetic field maximizes at postdusk/premidnight MLT hours, and the degree of the field line deformation can be quite significant well inside of the geosynchronous orbit. In the above event the model field lines with footpoints around 56° (residing on the geomagnetic shell $L \sim 3.2$ under quiet conditions) have been stretched to 6–7 R_E and formed a nearly tail-like configuration. The model polar cusps at that time shifted far equatorward so that their footpoints were found at geomagnetic latitudes ∼64°. For the 31 March 2001 event, with the peak Dst = −410, the model yielded an even more dramatic stretch of the nightside field lines so that those with footpoint latitudes as low as 53° (quiet-time $L \sim 2.8$) mapped to geocentric distances ∼5 R_E. The dayside cusp footpoints in that case moved to ∼63°. While only these two extreme events were analyzed in detail here, they clearly demonstrate the severe distortion of the inner magnetosphere. A more comprehensive analysis is planned for the near future to quantify the evolution of the inner magnetospheric configuration in the course of specific storms of different magnitude.

[59] The results presented here provide a quantitative answer to the question on the cause of the abnormally low latitudes of auroral displays during major space storms. Another related problem is the mechanism for a sudden appearance of relativistic particles deep in the inner magnetosphere [e.g., *Baker et al.*, 1998]. The enormous stretching of the inner geomagnetic field lines at the maximum phase of a storm implies a possibility of an injection of particles onto low L-shells and their concurrent "slingshot" energization by the Fermi/betatron mechanisms.

[60] Finally, our results have an important implication for particle simulations of the inner magnetospheric dynamics during major storms. In any such simulation, using a dipolar or quasi-dipolar magnetic field model even at $L \sim 3-4$ is inadequate. The magnetic field should be obtained either using a more realistic empirical model or by means of a fully self-consistent code, based on global particle distributions and externally driven boundary conditions.

References

Baker, D. N., et al., A strong CME-related magnetic cloud interaction with the Earth's magnetosphere: ISTP observations of rapid relativistic electron acceleration on May 15, 1997, *Geophys. Res. Lett.*, *25*, 2975, 1998.

Liemohn, M. W., J. U. Kozyra, M. F. Thomsen, J. L. Roeder, G. Lu, J. E. Borovsky, and T. E. Cayton, Dominant role of the asymmetric ring current in producing the stormtime Dst, *J. Geophys. Res.*, *106*, 883, 2001.

Meng, C.-I., Case studies of the storm time variation of the polar cusp, *J. Geophys. Res.*, *137*, 137, 1983.

Press, W. H., S. A. Teukolsky, W. T. Vetterling, and B. P. Flannery, *Numerical Recipes*, 2nd ed., Cambridge Univ. Press, New York, 1992.

Raeder, J., Y. L. Wang, T. J. Fuller-Rowell, and H. J. Singer, Global simulation of magnetospheric space weather effects of the Bastille Day storm, *Sol. Phys.*, *204*, 323, 2001.

Reiff, P. H., and J. G. Luhmann, Solar wind control of the polar cap potential, in *Solar Wind-Magnetosphere Coupling*, edited by Y. Kamide and J. A. Slavin, p. 453, Terra Sci., Tokyo, 1986.

Reiff, P. H., R. W. Spiro, and T. W. Hill, Dependence of the polar cap potential drop on interplanetary parameters, *J. Geophys. Res.*, *86*, 7639, 1981.

Shue, J.-H., P. Song, C. T. Russell, J. T. Steinberg, J. K. Chao, G. Zastenker, O. L. Vaisberg, S. Kokubun, H. J. Singer, T. R. Detman, and H. Kawano, Magnetopause location under extreme solar wind conditions, *J. Geophys. Res.*, *103*, 17,691, 1998.

Sibeck, D. G., R. B. Decker, D. G. Mitchell, A. J. Lazarus, R. P. Lepping, and A. Szabo, Solar wind preconditioning in the flank foreshock: IMP 8 observations, *J. Geophys. Res.*, *106*, 21,675, 2001.

Stauning, P., and F. Primdahl, First detection of global dawn-dusk ionospheric current intensities using Ampere's integral law on Ørsted satellite orbits, *Geophys. Res. Lett.*, *27*, 3273, 2000.

Tsyganenko, N. A., Modeling the Earth's magnetospheric magnetic field confined within a realistic magnetopause, *J. Geophys. Res.*, *100*, 5599, 1995.

Tsyganenko, N. A., Effects of the solar wind conditions on the global magnetospheric configuration as deduced from data-based field models, *Eur. Space Agency Spec. Publ., ESA SP-389*, 181, 1996.

Tsyganenko, N. A., A model of the near magnetosphere with a dawn-dusk asymmetry: 1. Mathematical structure, *J. Geophys. Res.*, *107*(A8), 1179, doi:10.1029/2001JA000219, 2002a.

Tsyganenko, N. A., A model of the near magnetosphere with a dawn-dusk asymmetry: 2. Parameterization and fitting to observations, *J. Geophys. Res.*, *107*(A8), 1176, doi:10.1029/2001JA000220, 2002b.

————————————

J. C. Kasper, Center for Space Research, Massachusetts Institute of Technology, Cambridge, MA 02139, USA. (jck@mit.edu)

H. J. Singer, National Oceanic and Atmospheric Administration, Space Environment Center, Boulder, CO 80305, USA. (Howard.Singer@noaa. gov)

N. A. Tsyganenko, Universities Space Research Association, Code 695, Laboratory for Extraterrestrial Physics, NASA Goddard Space Flight Center, Greenbelt, MD 20771, USA. (Nikolai.Tsyganenko@gsfc.nasa.gov)